A hybrid numerical simulation of isotropic compressible turbulence

J. Wang [a], L.-P. Wang [a,b,*], Z. Xiao [a], Y. Shi [a], S. Chen [a,c,**]

[a] State Key Laboratory of Turbulence and Complex Systems, Center for Applied Physics and Technology, College of Engineering, Peking University, Beijing 100871, PR China
[b] Department of Mechanical Engineering, University of Delaware, Newark, DE 19716, USA
[c] Department of Mechanical Engineering, The Johns Hopkins University, Baltimore, MD 21218, USA

ARTICLE INFO

ABSTRACT

A novel hybrid numerical scheme with built-in hyperviscosity has been developed to address the accuracy and numerical instability in numerical simulation of isotropic compressible turbulence in a periodic domain at high turbulent Mach number. The hybrid scheme utilizes a 7th-order WENO (Weighted Essentially Non-Oscillatory) scheme for highly compressive regions (i.e., shocklet regions) and an 8th-order compact central finite difference scheme for smooth regions outside shocklets. A flux-based conservative and formally consistent formulation is developed to optimize the connection between the two schemes at the interface and to achieve a higher computational efficiency. In addition, a novel numerical hyperviscosity formulation is proposed within the context of compact finite difference scheme for the smooth regions to improve numerical stability of the hybrid method. A thorough and insightful analysis of the hyperviscosity formulation in both Fourier space and physical space is presented to show the effectiveness of the formulation in improving numerical stability, without compromising the accuracy of the hybrid method. A conservative implementation of the hyperviscosity formulation is also developed. Combining the analysis and test simulations, we have also developed a criterion to guide the specification of a numerical hyperviscosity coefficient (the only adjustable coefficient in the formulation). A series of test simulations are used to demonstrate the accuracy and numerical stability of the scheme for both decaying and forced compressible turbulence. Preliminary results for a high-resolution simulation at turbulent Mach number of 1.08 are shown. The sensitivity of the simulated flow to the detail of thermal forcing method is also briefly discussed.

© 2010 Elsevier Inc. All rights reserved.

1. Introduction

Compressible turbulence is of importance to a large number of industrial applications and natural phenomena, including high-temperature reactive flows in heat engines, development of transonic and hypersonic aircrafts, inter-planet space exploration, solar winds, and star-forming clouds in galaxies. With increasing computational resources, direct numerical simulations of incompressible turbulent flows have been routinely conducted for many canonical boundary conditions

* Corresponding author at: Department of Mechanical Engineering, University of Delaware, Newark, DE 19716, USA. Tel.: +1 302 831 8160; fax: +1 302 831 3619.
** Corresponding author at: State Key Laboratory of Turbulence and Complex Systems, Center for Applied Physics and Technology, College of Engineering, Peking University, Beijing 100871, PR China. Tel.: +86 10 6275 7426; fax: +86 10 6275 7427.
E-mail addresses: lwang@udel.edu (L.-P. Wang), syc@pku.edu.cn (S. Chen).

and geometries. Similar developments for compressible flows are desired in order to provide parameterizations needed for modeling complex compressible turbulence in relevant applications.

While the pesudo-spectral method for incompressible isotropic homogeneous turbulence in a periodic domain has been well established [1,2], such a standard method is no longer suitable for compressible turbulence at high Mach numbers due to discontinuities associated with highly compressed flow regions (*i.e.*, shocklets). Pioneered by Lele [3], high-order compact finite difference (FD) scheme has gained popularity in computational fluid dynamics [4–8]. Earlier simulations for weakly compressible turbulence often utilized the compact FD scheme for all regions in the flow field. For example, Samtaney et al. [9] applied the compact FD scheme to direct numerical simulation of decaying compressible turbulence at low and moderate turbulent Mach numbers. The compact FD algorithm has spectral-like spatial resolution and its order can be varied. However, it cannot capture shocklets with typical grid resolution and could lead to numerical instability due to Gibbs oscillations. One popular and efficient class of numerical schemes to capture shocks without numerical instability is the ENO (Essentially Non-Oscillatory) scheme and its improved version WENO (Weighted Essentially Non-Oscillatory) scheme [10–12]. However, for direct numerical simulation of compressible turbulence, WENO is known to be highly dissipative for flow regions outside shocklets leading to unphysical energy spectrum at small scales [13].

A better approach is then to combine the compact FD and WENO (so-called the hybrid scheme). In such a hybrid approach, the WENO scheme is only used for a finite region (i.e., the shock region) from a shock front. In the remaining shock-free (i.e., smooth) regions the compact FD is employed instead. Several general issues arise: (1) How to correctly identify a shocklet front? (2) How many grid points should be used to cover the shock region or equivalently where to place the interface between WENO and compact FD treatments? and (3) How to smoothly switch between the WENO and the compact FD scheme at the interface?

To the authors' knowledge, there are a very few studies [14–17] in which a hybrid compact FD-WENO scheme had been applied for numerical simulation of shock–turbulence interaction problems or compressible turbulence containing shocklets. Adams and Shariff [14] developed a hybrid scheme by combining compact upwind FD and ENO to treat advection terms and they applied their method to interactions of shocks with prescribed fluctuations in one and two spatial dimensions. They simply used the magnitude of local gradient of solution variables to capture shocks. Pirozzoli [15] combined compact upwind FD and WENO to handle advection terms for inviscid Euler equation using a conservative formulation. In his approach, the resulting matrix could contain abrupt change (*i.e.*, without smooth transition) at the interface between WENO and compact FD. He used the magnitude of the difference of computed solution variable on adjacent grid points to capture shocks and applied his method to interaction of a prescribed planar shock with 3D isotropic turbulence as well as several other 1D and 2D shock wave problems. Ren et al. [16] introduced a complex weight function to gradually switch between compact upwind FD and WENO at the interface. They combined the differences of solution variables to detect shocks and tested their method for Euler equations and shock–vortex interactions in 1D and 2D. Zhou et al. [17] introduced a new family of compact upwind FD and combined this with WENO. They refined the shock-capture method of Ren et al. [16] to avoid incorrect inclusion of smooth waves in shock detection, but their additional shock-capture criterion involved four adjustable parameters. They applied their scheme to decaying compressible turbulence studied by Samtaney et al. [9]. Larsson et al. [13] demonstrated that a hybrid approach combining high-order central difference and WENO performed much better than the WENO scheme alone for decaying compressible isotropic turbulence. There are also several other studies that combine the usual, non-compact FD scheme and WENO [18,19,13,20], but they have the very similar issues in shock detection and the interface treatments as discussed above.

In this study, we intend to develop further and optimize the hybrid compact FD-WENO scheme in the following areas. First, we incorporated an efficient and accurate shock-capture scheme initially developed by Samtaney et al. [9] for the purpose of postprocessing of their compressible turbulence field. This capture scheme is based on the local compression as determined by the local dilatation magnitude. Physically, we believe that regions of highly negative dilatation are precisely the regions of severe discontinuity that require the special WENO treatment, as indicated in [13,20]. Previously, most studies applied a geometric jump condition to capture shocks, which may overestimate shock regions as strong turbulent fluctuations may be incorrectly treated as shocklets. Second, we bridged the compact FD and WENO at the interface using a conservative formulation to ensure physical conservation principles and numerical stability. Computationally, WENO is more expensive than compact FD. However, only a small percentage of the physical domain (typically less than 15%) is handled by WENO, the overall computational cost is not significantly increased. We also re-formulated the WENO scheme so it is formally consistent with the compact FD. Third, in smooth regions, a novel numerical hyperviscousity formulation is proposed to enhance numerical stability without compromising numerical accuracy. These improvements together will allow us to simulate turbulent compressible flows at relatively high turbulent Mach numbers and turbulent Reynolds numbers.

The paper is organized as follows. We will first present the physical governing equations and parameters for compressible turbulence in a periodic domain in Section 2. The main developments of the hybrid schemes are described in Section 3, including the hybrid formulation, large-scale forcing method, and numerical hyperviscosity formulation. Also shown in Section 3 is a thorough and insightful analysis of our hyperviscosity formulation in both Fourier space and physical space. A series of numerical tests are then shown in Section 4 to illustrate the novelty and capabilities of our hybrid schemes. Finally, main conclusions are summarized in Section 5.

2. Governing equations for compressible turbulent flow

In this study we consider a compressible turbulence of an ideal gas driven and maintained by large-scale momentum forcing and thermal forcing. The kinetic energy cascade from large to small scales requires energy input through forcing at the large scales, to balance the viscous dissipation at the small scales. At the same time, the viscous dissipation is converted to thermal energy or heating at the small scales, and therefore, we need to remove thermal energy at the large scales through forcing.

There are strong two-way couplings between the velocity field and thermal or temperature field in compressible turbulent flows. The thermal field affects the density, pressure, and fluid viscosity and therefore influences the local mass and momentum conservations. At the same time, the velocity field generates convective transport, pressure work, and local viscous heating affecting the evolution of the thermal field. Therefore, the dynamics is more complicated than the much well studied incompressible fluid turbulence. Specifically, the possible occurrence of localized shocklets in the flow field at moderate to high turbulent Mach numbers is a manifestation of such strong coupling.

The governing equations are written in dimensionless form, by introducing the following scales, U for velocity, L for length, L/U for time, T_0 for temperature, ρ_0 for density, c_0 for the speed of sound, $\rho_0 U^2$ for energy per unit volume, $p_0 \equiv \rho_0 c_0^2/\gamma$ for pressure, μ_0 for dynamic viscosity, and κ_0 for conductivity. Here $\gamma \equiv C_p/C_v$ is the ratio of specific heat at constant pressure C_p to that at constant volume C_v. We shall assume that both specific heats are independent of the temperature, which is a reasonable assumption for air for the temperature range encountered in this study (see below for further detail). For an ideal gas, the speed of sound $c_0 = \sqrt{\gamma R T_0}$, where R is the specific gas constant. The system is then governed by five dimensionless parameters: a Reynolds number $Re \equiv \rho_0 U L/\mu_0$, a Prandtl number $Pr \equiv \mu_0 C_p/\kappa_0$, a Mach number $M \equiv U/c_0$, γ, and $C_p T_0/c_0^2$. However, for an ideal gas, $R = C_p - C_v$, the last parameter is equal to $1/(\gamma - 1)$ and thus is not independent.

The dimensionless field variables, density ρ, pressure p, temperature T, and vector velocity u_i, are solved by the mass, momentum, and energy equations for a compressible fluid, plus the ideal gas equation of state. They can be written as

$$\frac{\partial \rho}{\partial t} + \frac{\partial(\rho u_j)}{\partial x_j} = 0, \tag{1}$$

$$\frac{\partial(\rho u_i)}{\partial t} + \frac{\partial[\rho u_i u_j + p_m \delta_{ij}]}{\partial x_j} = \frac{1}{Re}\frac{\partial \sigma_{ij}}{\partial x_j} + \mathcal{F}_i, \tag{2}$$

$$\frac{\partial \mathcal{E}}{\partial t} + \frac{\partial[(\mathcal{E} + p_m)u_j]}{\partial x_j} = \frac{1}{\alpha}\frac{\partial}{\partial x_j}\left(\kappa \frac{\partial T}{\partial x_j}\right) + \frac{1}{Re}\frac{\partial(\sigma_{ij}u_i)}{\partial x_j} - \Lambda + \mathcal{F}_j u_j, \tag{3}$$

$$p = \rho T, \tag{4}$$

where the modified pressure p_m, viscous stress σ_{ij}, and total energy (internal plus kinetic energy) per unit volume $\mathcal{E}$ are

$$p_m \equiv \frac{p}{\gamma M^2}, \quad \sigma_{ij} = \mu\left(\frac{\partial u_i}{\partial x_j} + \frac{\partial u_j}{\partial x_i}\right) - \frac{2}{3}\mu\theta\delta_{ij}, \tag{5}$$

$$\mathcal{E} = \frac{p}{(\gamma - 1)\gamma M^2} + \frac{1}{2}\rho(u_j u_j). \tag{6}$$

Here $\theta \equiv \partial u_k/\partial x_k$ is the dilatation. In writing the above momentum equation, the Stokes assumption relating the bulk viscosity to the shear viscosity has been applied. The dimensionless large-scale forcing per unit volume to the fluid momentum is denoted by $\mathcal{F}_i$, and the dimensionless large-scale heat sink or cooling function per unit volume is denoted by Λ. The coefficient α comes from nondimensionalization and is equal to $Pr Re(\gamma - 1)M^2$. The system shall be completed by specifying the dimensionless viscosity μ and dimensionless thermal conductivity κ.

For an ideal gas, the viscosity increases with temperature, which introduces an additional effect of thermal field on the velocity field. A reasonable power-law approximation for this temperature dependence, in dimensionless form, is [9]

$$\mu = T^{0.76}. \tag{7}$$

For the simulations considered in this study, the dimensionless temperature varies in the range of 0.55–3. Take air, for example, with reference dimensional viscosity $\mu_0 = 1.716 \times 10^{-5}$ kg/(m s) at the reference temperature of $T_0 = 273.15$ K, it is straightforward to verify that the above power-law approximation has a maximum relative error of about 5% for the extreme cases of $T \to 0.55$ and $T \to 3.0$. A better relation for an ideal gas would be the Sutherland's law [21], which can be written in dimensionless form using the same reference temperature and viscosity as

$$\mu = \frac{1.4042 T^{1.5}}{T + 0.40417}. \tag{8}$$

Again using measured viscosity data for air, it can be shown that this second relation has a maximum relative error of 2.0% at $T = 3$ and less than 0.52% at $T = 0.55$. Since the Sutherland's law is more accurate, we shall adopt the Sutherland's law in this study, instead of the power-law relation used in the previous work of Samtaney et al. [9].

To consider the temperature dependence of conductivity, we shall further assume that the actual Prandtl number $\mu\mu_0 C_p/(\kappa\kappa_0) = Pr\mu/\kappa$ is not sensitive to temperature change, which is reasonable for air for the range of temperature considered in this study. It follows then that the dimensionless conductivity can be described by the same Sutherland's law as

$$\kappa = \frac{1.4042T^{1.5}}{T + 0.40417}. \tag{9}$$

In this study, we set the reference Prandtl number $Pr = \mu_0 C_p/\kappa_0$ to 0.7 and ratio of specific heats $\gamma = 1.4$.

For later discussions, it would be useful to separate the kinetic energy $\mathcal{E}_K \equiv \rho u_j u_j/2$ and internal energy $\mathcal{E}_I \equiv \rho T/[(\gamma-1)\gamma M^2]$. The governing equation for $\mathcal{E}_K$ is

$$\frac{\partial \mathcal{E}_K}{\partial t} + \frac{\partial(\mathcal{E}_K u_j)}{\partial x_j} = -u_j\frac{\partial p_m}{\partial x_j} + \frac{1}{Re}u_i\frac{\partial \sigma_{ij}}{\partial x_j} + \mathcal{F}_j u_j, \tag{10}$$

where terms on the right hand side represent rate of work due to pressure gradient and viscous stress gradient, and the energy input due to forcing. The governing equation for $\mathcal{E}_I$ takes the form

$$\frac{\partial \mathcal{E}_I}{\partial t} + \frac{\partial(\mathcal{E}_I u_j)}{\partial x_j} = -p_m\theta + \frac{1}{\alpha}\frac{\partial}{\partial x_j}\left(\kappa\frac{\partial T}{\partial x_j}\right) + \frac{1}{Re}\sigma_{ij}\frac{\partial u_i}{\partial x_j} - \Lambda, \tag{11}$$

where the terms on the right hand side are the pressure compression work, heat diffusion, the viscous dissipation, and the cooling rate.

In this study an isotropic homogeneous flow in a periodic domain is considered. If the spatial average, denoted by $\langle\cdots\rangle$, over the periodic domain is applied to the above energy equations, we would have

$$\frac{\partial\langle\mathcal{E}_K\rangle}{\partial t} = \langle p_m\theta\rangle - \frac{1}{Re}\left\langle\sigma_{ij}\frac{\partial u_i}{\partial x_j}\right\rangle + \langle\mathcal{F}_j u_j\rangle, \tag{12}$$

$$\frac{\partial\langle\mathcal{E}_I\rangle}{\partial t} = -\langle p_m\theta\rangle + \frac{1}{Re}\left\langle\sigma_{ij}\frac{\partial u_i}{\partial x_j}\right\rangle - \langle\Lambda\rangle, \tag{13}$$

In the wavenumber space, the essential dynamics of the simulated compressible flow involves transfer of kinetic energy from large to small scales, and, at the same time, transfer of internal energy, primarily through the viscous dissipation, from small to large scales. It is important to note that the viscous dissipation is always positive and thus converting local kinetic energy to internal energy. On the other hand, the pressure term in the internal energy equation is positive in regions where the fluid is compressed but is negative when the local fluid volume expands. For the whole system, if both velocity and thermal fields are statistically stationary, we must have

$$\overline{\langle\mathcal{F}_j u_j\rangle} - \overline{\langle\Lambda\rangle} = 0, \tag{14}$$

where the overline represents time average. Namely, the kinetic energy added to the velocity field is balanced by the cooling rate.

We now briefly define important parameters characterizing the compressible turbulence. The r.m.s. component fluctuating velocity u' and the three-dimensional energy spectrum are defined as

$$\frac{3}{2}u'^2 = \frac{1}{2}\langle\mathbf{u}(\mathbf{x},t)\cdot\mathbf{u}(\mathbf{x},t)\rangle = \int_0^\infty E(k)dk. \tag{15}$$

The kinetic energy spectrum $E(k)$ can be computed by summing the modal kinetic energy $|\hat{u}|^2(\mathbf{k},t)/2$ from all modes with wavevector in a unit spherical shell in the wavevector space, defined by $k - 0.5 < |\mathbf{k}| \leqslant k + 0.5$. Likewise, the energy spectrum per unit volume is defined as

$$\langle\mathcal{E}_K\rangle = \frac{1}{2}\langle\rho\mathbf{u}(\mathbf{x},t)\cdot\mathbf{u}(\mathbf{x},t)\rangle = \int_0^\infty E_K(k)dk. \tag{16}$$

The longitudinal integral length scale L_f, namely, the integral time for radial two-point velocity correlation, can be computed in terms of $E(k)$, as [22]

$$L_f = \frac{\pi}{2u'^2}\int_0^\infty \frac{E(k)}{k}dk. \tag{17}$$

The transverse Taylor microscale λ and Taylor microscale Reynolds number Re_λ are defined as:

$$\lambda = \frac{u'}{\langle[(\partial u_1/\partial x_1)^2 + (\partial u_2/\partial x_2)^2 + (\partial u_3/\partial x_3)^2]/3\rangle^{1/2}}, \quad Re_\lambda = \frac{u'\lambda\langle\rho\rangle}{\langle\mu\rangle}, \tag{18}$$

where the longitudinal average gradient squared is averaged over the three spatial directions to improve its statistical estimate. The average normalized viscous dissipation rate is computed as

$$\epsilon = \frac{1}{Re}\left\langle \frac{\sigma_{ij}}{\rho}\frac{\partial u_i}{\partial x_j}\right\rangle. \tag{19}$$

Kolmogorov length scale is defined as

$$\eta = [\langle \mu/\rho\rangle^3/\epsilon]^{1/4}. \tag{20}$$

Finally, the turbulent Mach number M_t is given as [9]

$$M_t = M\frac{\langle u_1^2 + u_2^2 + u_3^2\rangle^{1/2}}{\langle\sqrt{T}\rangle}. \tag{21}$$

3. The hybrid computational approach

3.1. The consistent conservative formulation

Specifically, we combined an eighth-order compact central FD scheme [3] for smooth regions with a seventh-order WENO scheme [12] for the shock regions to treat the advection terms in the governing equations. To begin this process, we identify the shock front by spatial points with highly negative local dilatation as defined by $\theta < -R_\theta\theta'$ [9], where R_θ is set to 3.0 unless otherwise noted.[1] Then the shock region treated by WENO includes the shock front and additional six[2] grid points on both left and right in each spatial direction immediately outside the front. Then the grid points starting from the seventh point on from the shock front define the smooth region. The half grid location between the sixth and the seventh grid points is referred to as the joint or the interface location. Since the fluxes (to be introduced below) will be defined at half grid points, this joint will require a special treatment.

Next, to illustrate our reformulation of the hybrid scheme, we express the eighth-order compact central FD scheme as [3]:

$$\alpha_1 f'_{j-1} + f'_j + \alpha_1 f'_{j+1} = a_1\frac{f_{j+1}-f_{j-1}}{h} + b_1\frac{f_{j+2}-f_{j-2}}{h} + c_1\frac{f_{j+3}-f_{j-3}}{h}, \tag{22}$$

where the prime indicates spatial derivative in a given direction, h is the grid spacing, and

$$\alpha_1 = \frac{3}{8}, \quad a_1 = \frac{25}{32}, \quad b_1 = \frac{1}{20}, \quad c_1 = -\frac{1}{480}. \tag{23}$$

In the conservative formulation, we can recast Eq. (22) as follows [15]

$$\alpha_1 f'_{j-1} + f'_j + \alpha_1 f'_{j+1} = \frac{F^{\text{Compact}}_{j+1/2} - F^{\text{Compact}}_{j-1/2}}{h}, \tag{24}$$

where

$$F^{\text{Compact}}_{j+1/2} = c_1(f_{j+3}+f_{j-2}) + (b_1+c_1)(f_{j+2}+f_{j-1}) + (a_1+b_1+c_1)(f_{j+1}+f_j). \tag{25}$$

On the other hand, a seventh-order WENO scheme can be formally written as

$$f'_j = \frac{f^{\text{WENO}}_{j+1/2} - f^{\text{WENO}}_{j-1/2}}{h}. \tag{26}$$

Further details can be found in [12]. To make it completely consistent to the compact FD formulation in Eq. (24), we can re-write Eq. (26) as

$$\alpha_1 f'_{j-1} + f'_j + \alpha_1 f'_{j+1} = \frac{F^{\text{WENO}}_{j+1/2} - F^{\text{WENO}}_{j-1/2}}{h} \tag{27}$$

with

$$F^{\text{WENO}}_{j+1/2} \equiv \alpha_1 f^{\text{WENO}}_{j+3/2} + f^{\text{WENO}}_{j+1/2} + \alpha_1 f^{\text{WENO}}_{j-1/2}. \tag{28}$$

This then naturally allows us to use one single formulation in the whole domain, namely,

$$\alpha_1 f'_{j-1} + f'_j + \alpha_1 f'_{j+1} = \frac{F^{\text{Hybrid}}_{j+1/2} - F^{\text{Hybrid}}_{j-1/2}}{h} \tag{29}$$

---

[1] It will be shown in Section 4.6 that the results are rather insensitive to the value of R_θ chosen when $1 \leqslant R_\theta \leqslant 4$.

[2] This number can be reduced to three, as three grid points are adequate to support the compact FD schemes used for the smooth region just outside the joint. Our test simulations show no difference if the number of grid points on each side of the shock front used to define the shock region varies from three to six.

with,

$$
F_{j+1/2}^{\text{Hybrid}} \equiv \begin{cases}
F_{j+1/2}^{\text{Compact}} & \text{for smooth regions,} \\
F_{j+1/2}^{\text{WENO}} & \text{for shock regions,} \\
\frac{1}{2}\left(F_{j+1/2}^{\text{Compact}} + F_{j+1/2}^{\text{WENO}}\right) & \text{at the joint.}
\end{cases}
\tag{30}
$$

Here the flux at the joint is naturally taken as the average of the fluxes on two sides of the joint. The above reformulation greatly simplifies the coding and allows us to take full advantage of the periodic boundary conditions. In each spatial direction, the computation of spatial derivatives amounts to solving N^2 tridiagonal systems in parallel, where N is the grid resolution in each direction.

For computational efficiency, the viscous term in the momentum equation was handled by a non-compact sixth-order central FD scheme since the non-compact FD scheme is fully explicit. This does not affect the accuracy of the numerical solution since the viscous term is typically smaller than the advection term by 3 orders of magnitude. The same method was used for the viscous dissipation term in the energy equation.

Since the thermal diffusion term in the energy equation carries several other parameters, see Eq. (3), it is treated by a non-hybrid but higher-order (eighth-order) compact FD scheme [3].

Finally, the time marching is performed by an explicit low storage second-order Runge–Kutta technique [10,23]. The third-order Runge–Kutta scheme was also tested and no significant difference in results was found. The time step size was determined based on a conservative CFL number criterion, following the definition of Adam and Shariff [14] for compressible flow simulation. Namely,

$$
\Delta t = \text{CFL} \times \frac{\Delta x}{[\max(|u_1| + c) + \max(|u_2| + c) + \max(|u_3| + c)]}.
\tag{31}
$$

Typically, we have a CFL number of 0.2 or less for decaying turbulence simulation and 0.5 or less for forced turbulence simulation. It will be shown later that doubling the time step size does not alter the results.

3.2. Large-scale forcing

Previous studies of compressible homogeneous isotropic turbulence considered both decaying compressible turbulence [9,24,25] and forced stationary compressible turbulence [26,27]. Since both energy and momentum must be considered together, a stationary flow requires a separate forcing scheme for the thermal field in addition to the more conventional forcing applied to the velocity field.

As indicated above, we consider a compressible turbulence with kinetic energy input at the large scales and this energy is converted into the internal energy at the small viscous scales. This will have to be removed by large-scale thermal cooling.

Similar to forcing incompressible turbulence [28], the momentum forcing field is constructed in the Fourier space by fixing the kinetic energy $E(k)$ per unit mass within the two lowest wave number shells, $0.5 < |\mathbf{k}| \leqslant 1.5$ and $1.5 < |\mathbf{k}| \leqslant 2.5$, to prescribed values consistent with the $k^{-5/3}$ kinetic energy spectrum. This is performed as follows. First, we transform the velocity field $\mathbf{u}(\mathbf{x}, t)$ into the Fourier space to yield $\mathbf{v}(\mathbf{k}, t)$. Next, we decompose this field into a divergence-free field (part I) and divergence-containing field (part II) as

$$
\mathbf{v}(\mathbf{k}, t) = \mathbf{v}^{\text{I}}(\mathbf{k}, t) + \mathbf{v}^{\text{II}}(\mathbf{k}, t),
\tag{32}
$$

where

$$
\mathbf{v}^{\text{I}}(\mathbf{k}, t) = \mathbf{v}(\mathbf{k}, t) - \frac{\mathbf{k}\mathbf{k} \cdot \mathbf{v}}{k^2},
\tag{33}
$$

$$
\mathbf{v}^{\text{II}}(\mathbf{k}, t) = \frac{\mathbf{k}\mathbf{k} \cdot \mathbf{v}}{k^2}.
\tag{34}
$$

Clearly the kinetic energy associated with each wave vector is also decomposed such that

$$
\frac{|\mathbf{v}(\mathbf{k}, t)|^2}{2} = \frac{|\mathbf{v}^{\text{I}}(\mathbf{k}, t)|^2}{2} + \frac{|\mathbf{v}^{\text{II}}(\mathbf{k}, t)|^2}{2}.
\tag{35}
$$

By summing over all modes belong to a given wavenumber shell, one can then calculate the kinetic energy in each of the first two wavenumber shells as

$$
E(0.5 \leqslant k < 1.5) = E^{\text{I}}(0.5 \leqslant k < 1.5) + E^{\text{II}}(0.5 \leqslant k < 1.5),
$$
$$
E(1.5 \leqslant k < 2.5) = E^{\text{I}}(1.5 \leqslant k < 2.5) + E^{\text{II}}(1.5 \leqslant k < 2.5).
$$

To maintain the total kinetic energy in the first two shells to prescribed levels $E(1)$ and $E(2)$, respectively, we amplify the divergence-free part of the velocity field such that, after the forcing,

$$
\mathbf{v}(\mathbf{k}, t) = \alpha \mathbf{v}^{\text{I}}(\mathbf{k}, t) + \mathbf{v}^{\text{II}}(\mathbf{k}, t),
\tag{36}
$$

where, for example, α for all the modes in the first wavenumber shell is set to

$$\alpha(0.5 \leqslant k < 1.5) = \sqrt{\frac{E(1) - E^{\mathrm{II}}(0.5 \leqslant k < 1.5)}{E^{\mathrm{I}}(0.5 \leqslant k < 1.5)}}. \tag{37}$$

In this manner, the velocity field after forcing has a total kinetic energy in the first wavenumber shell equal to the prescribed value of $E(1)$. The same procedure is applied to determine α for all the modes in the second wavenumber shell. This deterministic forcing maintains the energy levels in the two low wavenumber shells without changing the large-scale divergence field. Typically, we set $E(1) = 1.242477$ and $E(2) = 0.391356$. Therefore, the forcing field per unit mass in the physical space, namely, $\mathcal{F}_i/\rho$ in terms of the notation of Eq. (2), is then the inverse Fourier transform of $(\alpha - 1)\mathbf{v}^{\mathrm{I}}(\mathbf{k},t)$.

In addition, a thermal cooling function Λ is added to the energy equation, Eq. (3), at every time step to prevent the internal energy from increasing. This is more clearly shown in Eq. (11). We have considered three types of cooling function following Passot et al. [27]:

$$\Lambda_{\mathrm{I}} = \sigma_{\mathrm{I}}T^0, \quad \Lambda_{\mathrm{II}} = \sigma_{\mathrm{II}}T^2, \quad \Lambda_{\mathrm{III}} = \sigma_{\mathrm{III}}T^4, \tag{38}$$

where the first represents a uniform cooling in space, the third represents radiative cooling, and the second is somewhat in between. Our simulations show that the results are not sensitive to the type of cooling applied.

3.3. A novel model for numerical hyperviscosity

3.3.1. Motivation and formulation

During the development of our simulation code, we encountered a numerical instability problem due to occurrence of small scale fluctuations. Such small-scale fluctuations could originate from two sources. First, it is known that central FD scheme is not dissipative and tends to generate random fluctuations at small scales [6]. Second, even when two stable numerical schemes are patched together, small oscillations (noise) may be generated due to potential sharp transition of the two schemes at the interface [20]. For example, our experience indicates that, due to numerical issues at the interface, a hybrid treatment using compact upwind scheme and WENO can be unstable for moderate to high turbulent Mach numbers.

Here we propose a natural numerical viscosity treatment, in line with compact FD schemes, that will dissipate the unwanted small-scale fluctuations without compromising the accuracy of the scheme. The novel aspect of our implementation is that the numerical viscosity term has a high-order spatial structure similar to the discretization error of the overall numerical method. This is accomplished by taking the difference of two compact FD algorithms of second-order spatial derivatives. The first is based on a compact central FD applied to the first-order spatial derivatives, but applied twice to yield the second-order derivatives, while the second is a compact central FD applied directly to the second-order derivatives. The procedure we describe below can be applied to any compact central FD provided that the two algorithms for the first and second-order spatial derivatives share a same stencil width.

As a specific example, we first recognize the following eighth-order compact central FD scheme for the first-order spatial derivative [3]

$$\beta_2 f'_{j-2} + \alpha_2 f'_{j-1} + f'_j + \alpha_2 f'_{j+1} + \beta_2 f'_{j+2} = a_2 \frac{f_{j+1} - f_{j-1}}{h} + b_2 \frac{f_{j+2} - f_{j-2}}{h}, \tag{39}$$

where

$$\alpha_2 = \frac{4}{9}, \quad \beta_2 = \frac{1}{36}, \quad a_2 = \frac{20}{27}, \quad b_2 = \frac{25}{216}. \tag{40}$$

We then recognize the following compact FD scheme for the second-order derivative [3]

$$\beta_3 f''_{j-2} + \alpha_3 f''_{j-1} + f''_j + \alpha_3 f''_{j+1} + \beta_3 f''_{j+2} = a_3 \frac{f_{j+1} - 2f_j + f_{j-1}}{h^2} + b_3 \frac{f_{j+2} - 2f_j + f_{j-2}}{h^2}, \tag{41}$$

where

$$\alpha_3 = \frac{344}{1179}, \quad \beta_3 = \frac{38\alpha_3 - 9}{214},$$
$$a_3 = \frac{696 - 1191\alpha_3}{428}, \quad b_3 = \frac{1227\alpha_3 - 147}{1070}. \tag{42}$$

It is important to note that a same stencil width of five is used on both sides of Eqs. (39) and (41). For the reason of numerical stability, we will apply an implicit time-marching scheme to include numerical hyperviscosity term.

Before deriving the numerical viscosity formulation, we shall first apply the discrete Fourier transformation to both Eqs. (39) and (41). Consider a periodic domain in one dimension of size 2π and assume this domain is divided into N equal intervals with grid coordinates $x_j = 2\pi j/N$ with $j = 0, 1, 2, \ldots, N$. Denote $\zeta_k = 2\pi k/N$, the discrete Fourier transform is

$$f(x_j) \equiv f_j = \frac{1}{N} \sum_{k=-N/2+1}^{N/2} \hat{f}_k \exp\left(\frac{2\pi \imath k j}{N}\right) = \frac{1}{N} \sum_{k=-N/2+1}^{N/2} \hat{f}_k \exp(\imath j \zeta_k). \tag{43}$$

It is important to recognize that the spatial derivative obtained from Eq. (39) is not the exact spatial derivative, but rather one of the possible numerical approximations. For clarity, we now denote the numerical approximation of the first-order spatial derivative as f'_n, with the subscript n indicating a numerical approximation. The Fourier transform of the approximation f' from Eq. (39) is denoted by $\hat{f}'_n$. Then in the Fourier space, Eq. (39) becomes

$$\widehat{f'_{n},k} = \imath k \hat{f}_k \times s_1(\zeta_k), \tag{44}$$

where

$$s_1(\zeta_k) \equiv \frac{2a_2 \sin \zeta_k + 2b_2 \sin(2\zeta_k)}{\zeta_k[1 + 2\alpha_2 \cos \zeta_k + 2\beta_2 \cos(2\zeta_k)]}. \tag{45}$$

Likewise, denote the approximation f'' from Eq. (41) as f''_n and its Fourier transform as $\hat{f}''_n$, then we have

$$\widehat{f''_{n},k} = -k^2 \hat{f}_k \times s_2(\zeta_k), \tag{46}$$

where

$$s_2(\zeta_k) = \frac{2a_3[1 - \cos \zeta_k] + 2b_3[1 - \cos(2\zeta_k)]}{\zeta_k^2[1 + 2\alpha_3 \cos \zeta_k + 2\beta_3 \cos(2\zeta_k)]}. \tag{47}$$

The spectral-like accuracy of the compact FD schemes, Eqs. (39) and (41), can be stated equivalently as $s_1(\zeta_k) \approx 1$ and $s_2(\zeta_k) \approx 1$. This is the case for $\zeta_k < 2$, as shown in Fig. 1. Fig. 1 also shows that the direct calculation by scheme 2 is more accurate than the indirect scheme 1 for $\zeta_k > 2$. It is interesting to recast the above observation in the context of spectral simulation without explicit de-aliasing. In such a case, one normally applies the simple 2/3 rule and resolves the wavenumber up to $k = 2/3 k_{max} = 2/3 \times N/2 = 0.667 k_{max}$. The location $\zeta_k = 2$ corresponds to $k = N/\pi = 2/\pi \times k_{max} = 0.637 k_{max}$. This demonstrates that the eighth-order central compact FD yields essentially the same spectral accuracy as the pseudo-spectral method without explicit de-aliasing.

Fig. 1 also provides a novel mechanism for adding numerical hyperviscosity. Image that we add a term of the following form to the right hand side of a governing equation in Fourier space

$$\frac{d\hat{f}_k}{dt} = \text{other terms} - v_n k^2 \hat{f}_k \times [s_2(\zeta_k) - s_1^2(\zeta_k)], \tag{48}$$

where the coefficient v_n is an adjustable constant. The novelty of this numerical hyperviscosity-like term is connected to the following two observations: (1) $[s_2(\zeta_k) - s_1^2(\zeta_k)] \approx 0$ for $\zeta_k < 2$, meaning that there is no numerical diffusion for almost all resolved scales, and (2) $[s_2(\zeta_k) - s_1^2(\zeta_k)]$ is positive definite for all k. In other words, our numerical viscosity scheme introduces a scale-dependent viscosity that is equal to $v_n[s_2(\zeta_k) - s_1^2(\zeta_k)]$. Thus this numerical viscosity is negligible for almost all resolved scales and is always positive and increases monotonically with k at high wavenumbers. These observations clearly demonstrate that our proposed numerical viscosity scheme can efficiently remove any unphysical numerical oscillations at high wavenumbers without compromising the accuracy of the overall scheme.
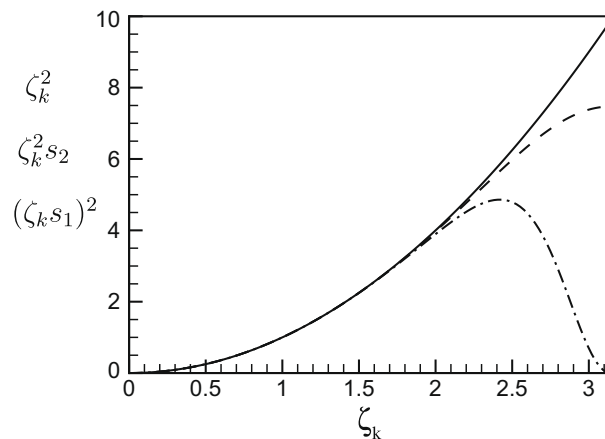

Fig. 1. Demonstration of spectral-like accuracy of the compact central FD schemes. Solid line represents the exact result which is equal to ζ_k^2; dash line is $\zeta_k^2 s_2$; dash dotted line is $(\zeta_k s_1)^2$.

3.3.2. Analysis and implications of the proposed model

To further understand the structure of the proposed numerical hyperviscosity formulation, we shall examine its limiting behaviors. First, as $\zeta_k \to 0$, we can rewrite s_1 and s_2 in the following format:

$$s_1(\zeta_k) = \frac{[2a_2 \sin \zeta_k + 2b_2 \sin(2\zeta_k)]/\zeta_k}{[1 + 2\alpha_2 \cos \zeta_k + 2\beta_2 \cos(2\zeta_k)]} = \frac{P_0 - P_2\zeta_k^2 + P_4\zeta_k^4 - P_6\zeta_k^6 + Q_8\zeta_k^8 - Q_{10}\zeta_k^{10} + \cdots}{P_0 - P_2\zeta_k^2 + P_4\zeta_k^4 - P_6\zeta_k^6 + P_8\zeta_k^8 - P_{10}\zeta_k^{10} + \cdots}, \tag{49}$$

and

$$s_2(\zeta_k) = \frac{\{2a_3[1 - \cos \zeta_k] + 2b_3[1 - \cos(2\zeta_k)]\}/\zeta_k^2}{1 + 2\alpha_3 \cos \zeta_k + 2\beta_3 \cos(2\zeta_k)} = \frac{P_0' - P_2'\zeta_k^2 + P_4'\zeta_k^4 - P_6'\zeta_k^6 + Q_8'\zeta_k^8 - Q_{10}'\zeta_k^{10} + \cdots}{P_0' - P_2'\zeta_k^2 + P_4'\zeta_k^4 - P_6'\zeta_k^6 + P_8'\zeta_k^8 - P_{10}'\zeta_k^{10} + \cdots}, \tag{50}$$

Note that for both s_1 and s_2, the first four terms in the numerator and the denominator (*i.e.*, up to term ζ_k^6) are identical in each case *by design*. In addition, the coefficients decrease quickly with the order and more precisely, they are $P_0 = 1.94444$, $P_2 = 5.55556e{-}1$, $P_4 = 7.40741e{-}2$, $P_6 = 6.17284e{-}3$, $P_8 = 3.74780e{-}4$, $P_{10} = 1.59220e{-}5$, $Q_8 = 3.30688e{-}4$, $Q_{10} = 1.19137e{-}5$, $P_0' = 1.60305$, $P_2' = 3.30789e - 1$, $P_4' = 3.73198e - 2$, $P_6' = 2.54453e - 3$, $P_8' = 1.38334e - 4$, $P_{10}' = 5.66573e - 6$, $Q_8' = 1.117439e - 4$, $Q_{10}' = 3.37598e - 6$. These imply that for small ζ_k, the leading order expansion for the effective viscosity is

$$v_n[s_2 - s_1^2] = v_n C(\zeta_k)\zeta_k^8 \approx v_n C(0)\zeta_k^8, \tag{51}$$

where $C(\zeta_k)$ is a dimensionless parameter and $C(0) \equiv C(\zeta_k = 0) = 2.876e{-}5$. Numerically we found that $C(\zeta_k)$ changes from $2.876e{-}5$ to $3.128e{-}5$ when ζ_k is varied from $\zeta_k = 0$ to $\zeta_k = 0.5$.

Fig. 2 confirms that $[s_2(\zeta_k) - s_1^2(\zeta_k)]$ is almost identical to $C(0)\zeta_k^8 = 2.876e - 5\zeta_k^8$ for the region $\zeta_k < 0.5$. The limiting behavior, in fact, is a reasonable approximation even for $\zeta_k = 1.0$ due to the rapid decrease of expansion coefficients in Eqs. (49) and (50). Note that the magnitude in Fig. 2 changes by 18 orders, a special care must be taken to compute the exact value of $[s_2 - s_1^2]$ at small ζ_k, namely, the leading order term in s_1 and s_2 must be dropped analytically before computing the difference. This large magnitude contrast implies the effectiveness of the hyperviscosity model on removing noises at the high wavenumbers without introducing much numerical viscosity at low and moderate wavenumbers. In the physical space the above asymptotic behavior implies, for large scales,

$$v_n[f_n'' - (f_n')_n'] \approx v_n C(0)(\Delta x)^8 (\nabla^2)^5 f, \tag{52}$$

which explicitly indicates the approximate form of the numerical hyperviscosity term in the physical space. Since we solve the governing equations, Eqs. (1)–(4), in dimensionless form, the values v_n should be interpolated as having been normalized by LU. Such a formulation introduces negligible viscosity for $\zeta_k \leqslant 1$ as long as

$$\frac{v_n C(0)}{\mu/Re} \ll 1. \tag{53}$$

The fact that the effective viscosity at the high wavenumber end is larger than the asymptotic line in Fig. 2 demonstrates that our formulation is more effective than the usual hyperviscosity model of the type given by Eq. (52). It should be noted that, even one specifies a hyperviscosity model according to Eq. (52) in the physical space, there is no guarantee that its numerical implementation will preserve the form due to numerical discretization errors. Such problem is avoided here since a related advantage of our formulation is that it is completely in line with the highly accurate compact FD schemes used to solve the governing equations.
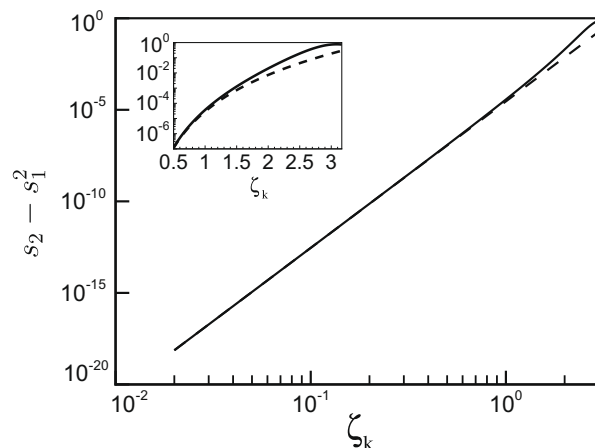

Fig. 2. The variation of effective numerical viscosity $[s_2(\zeta_k) - s_1^2(\zeta_k)]$ with normalized wavenumber ζ_k, as indicated by the solid line. Dashed line represents $C(0)\zeta_k^8$, see Eq. (51).

The above asymptotic analysis also implies that our hyperviscosity formulation can be generalized to compact central FD schemes of any other even orders.

In the other limit of $\zeta_k \to \pi$, $s_1 \to 0$ and

$$s_2 \to \frac{4a_3}{\pi^2[1 - 2\alpha_3 + 2\beta_3]} = 0.757, \tag{54}$$

which shows the effective viscosity applied to the highest wavenumber is $0.757\nu_n$.

3.3.3. Implementation

The numerical hyperviscosity term is simply implemented in physical space as

$$\frac{\partial f}{\partial t} = \text{other terms} + \nu_n[f_n'' - (f_n')_n']. \tag{55}$$

Numerical tests shown in Table 1, Figs. 3 and 4 will demonstrate that, as long as Eq. (53) is observed, results are insensitive to the value of ν_n used, even when ν_n is varied by more than two orders of magnitude. This is consistent with the earlier observation that the numerical hyperviscosity term makes a negligible contribution to the well resolved large scales. The overall accuracy of our numerical method will be demonstrated in Section 4 when comparing with the published results by Samtaney et al. [9] and those of standard pseudo-spectral simulations.

Since the main purpose of the numerical hyperviscosity term is to smooth out unwanted fluctuations at small scales that are not designed to be resolved, we add this numerical hyperviscosity term directly to five primary variables: density ρ, three components of velocity u, v, w, temperature T at the end of every five time steps with a step size of $5dt$, where dt is the time step size used for all physical terms. A same ν_n value was used for all these variables.

For the three-dimensional compressible flow, we implemented the numerical hyperviscosity term as follows:

$$\frac{\partial f}{\partial t} = \nu_n\{[f_{n,xx} - (f_{n,x})_{n,x}] + [f_{n,yy} - (f_{n,y})_{n,y}] + [f_{n,zz} - (f_{n,z})_{n,z}]\}, \tag{56}$$

where the subscript n again denotes numerical approximations and subscripts x, y, z denote spatial derivatives. For better numerical stability, the three terms $f_{n,xx}, f_{n,yy}$, and $f_{n,zz}$ in Eq. (56) are handled by the implicit Euler scheme. While for the other three terms with negative sign, it is not feasible to apply an implicit scheme so we simply used an explicit Euler scheme. Each term on the right hand side of Eq. (56) was added sequentially and in the same order as appeared in Eq. (56). Here the accuracy of time integration scheme is not relevant as the resolved large-scale fluctuations are not affected.

It must be pointed out that the numerical hyperviscosity term should not be applied to shock fronts. This is because shock fronts contain jumps and any compact FD scheme will cause Gibbs oscillations which will unfavorably affect the stability of WENO. We developed a consistent and conservative formulation to selectively omit numerical hyperviscosity in shock regions. To begin, we write Eqs. (39) and (41) in matrix form as

$$AF_n' = BF, \quad A(F_n')_n' = BF_n', \\ \text{or} \quad F_n' = A^{-1}BF, \quad (F_n')_n' = A^{-1}BF_n', \tag{57}$$

and

$$CF_n'' = DF \quad \text{or} \quad F_n'' = C^{-1}DF, \tag{58}$$

respectively, where A, B, C, and D are penta-diagonal matrices. For example, A is a penta-diagonal matrix with $\beta_2, \alpha_2, 1, \alpha_2, \beta_2$ as entries, with the third entry placed on the diagonal line, along with periodic wrapping in any given direction; B has $-b_2/h$, $-a_2/h$, 0, a_2/h, b_2/h as entries, and so on. Next, the B matrix can be splitted into two tetra-diagonal matrices $B_{+1/2}$ and $B_{-1/2}$, centered at $j + \frac{1}{2}$ and $j - \frac{1}{2}$, respectively. Here j denotes the diagonal line of the matrix. The entries for $B_{+1/2}$ and $B_{-1/2}$ are the same and equal to b_2/h, $(a_2 + b_2)/h$, $(a_2 + b_2)/h$, b_2/h. The similar decomposition can be done for D. Therefore, we have

$$(F_n')_n' = A^{-1}(B_{+1/2} - B_{-1/2})F_n' \equiv A^{-1}(G_{+1/2} - G_{-1/2}) \tag{59}$$

and

Table 1
Runs and parameters for decaying compressible turbulence.

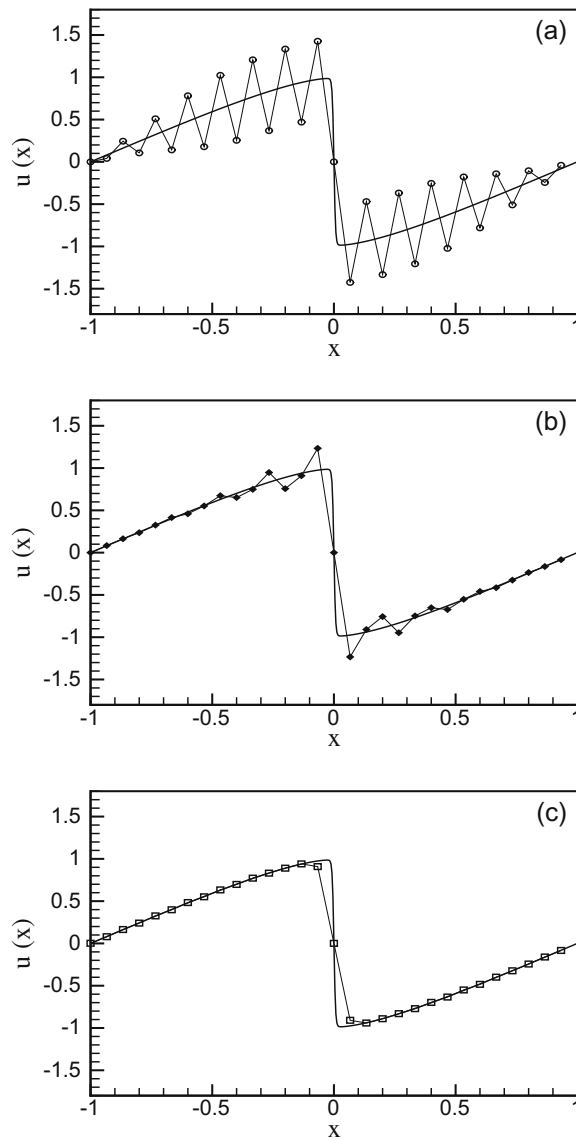| Run no.	Method	$Re_\lambda(0)$	$M_t(0)$	ν_n	dt/τ
128DC1	Compact	72	0.30	0.05	0.001
128DC2	Compact	72	0.30	0.05	0.002
128DC3	Compact	72	0.30	10.0	0.001
128DC4	Compact	72	0.56	0.05	0.001
128DH1	Hybrid	72	0.56	0.05	0.001
128DW1	WENO	72	0.56	–	0.001

Fig. 3. Solutions to 1D viscous Burgers' equation with an unresolved standing shock wave at $x = 0$ and $t = 0.5$: (a) compact FD solution without any hyperviscosity, (b) compact FD solution with $v_n = 1.0$, (c) the hybrid scheme with seven grid points defining the shock region. In all plots, the thick smooth solid line represents the exact analytical solution at the same time. Note that, for this particular example, due to the smooth nature of the solution outside the shock wave, the WENO alone gives a good solution for all regions.
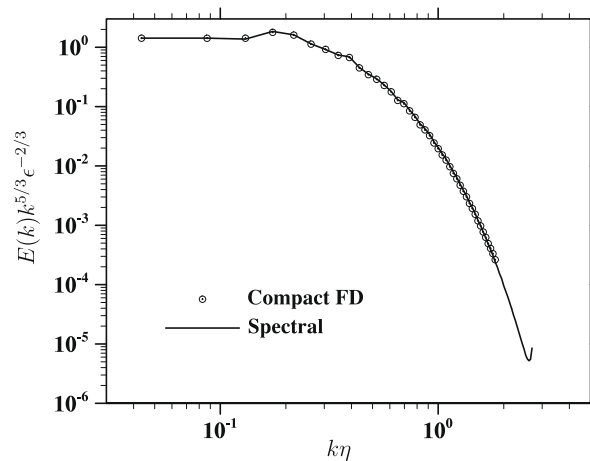
Fig. 4. Comparison of simulated kinetic energy spectrum with standard pseudo-spectral simulation for a forced isotropic turbulence at small turbulent Mach number $M_t = 0.236$ and $R_\lambda = 64.6$.

$$F''_n = C^{-1}(D_{+1/2} - D_{-1/2})F \equiv A^{-1}(H_{+1/2} - H_{-1/2}), \tag{60}$$

where

$$G_{+1/2} \equiv B_{+1/2}F'_n, \quad G_{-1/2} \equiv B_{-1/2}F'_n,$$
$$H_{+1/2} = AC^{-1}D_{+1/2}F, \quad H_{-1/2} = AC^{-1}D_{-1/2}F. \tag{61}$$

The above decomposition provides a conservative flux-like formulation, similar to Eq. (24). This flux formulation is further evidenced through the following shifting relations:

$$(G_{-1/2})_j = (G_{+1/2})_{j-1}, \quad (H_{-1/2})_j = (H_{+1/2})_{j-1}. \tag{62}$$

A simple switch is now introduced to seamlessly erase the hyperviscosity term in the shock region. The switch modifies G as follows:

$$(G_{+1/2})_j \equiv \begin{cases} (G_{+1/2})_j, & \text{smooth regions}; \\ (H_{+1/2})_j, & \text{shock regions}; \\ \frac{1}{2}[(G_{+1/2})_j + (H_{+1/2})_j], & \text{at the joint}. \end{cases} \tag{63}$$

Note that different j indices correspond to different locations relative to the shock region, so the switch may be turned on (shock regions) or off (smooth regions) depending on the value of j. The same switch is also applied to $G_{-1/2}$. With these modified $G_{+1/2}$ and $G_{-1/2}$, the numerical hyperviscosity term $v_n[F''_n - (F'_n)'_n]$ is unchanged in the smooth regions but reduces to zero in the shock regions.

4. Results and verification

In this section, we will present a series of numerical tests to demonstrate the capabilities of our hybrid method, especially the accuracy and numerical stability of our method.

4.1. Rigorous test results for 1D problem

We first test our hybrid scheme for a standard 1D viscous Burgers' equation

$$\frac{\partial u}{\partial t} + u\frac{\partial u}{\partial x} = v\frac{\partial^2 u}{\partial x^2} \tag{64}$$

in a periodic domain of $-1 \leqslant x \leqslant 1$, with an initial condition of $u(x, t = 0) = -\sin(x)$. The physical viscosity is set to $v = 0.01/\pi$ and the 1D domain is discretized by only 30 equal intervals (grid spacing $\Delta x = 1/15$). In the above, we implicitly assume that all properties have been normalized. A standing shock wave will appear at $x = 0$ due to compression from both sides. The flow outside the shock wave is rather smooth. The thickness of the shock wave scaled roughly with v, which is much less than Δx. Therefore, the shock wave is not resolved by the grid and Gibbs oscillations will occur if WENO is not employed.

The analytical solution for this 1D problem is

$$u(x, t) = -\frac{\int_{-\infty}^{\infty} \sin[\pi(x - \eta)]f(x - \eta)\exp(-\eta^2/4vt)d\eta}{\int_{-\infty}^{\infty} f(x - \eta)\exp(-\eta^2/4vt)d\eta}, \tag{65}$$

where $f(y) \equiv \exp[-\cos(\pi y)/2\pi v]$. The Gauss–Hermite integration with up to 30 terms are used to compute the above exact solution, which is shown in Fig. 3 by the thick smooth solid line.

In Fig. 3 we compare solutions from different numerical methods with the analytical solution at $t = 0.5$ when the shock has been fully formed. Clearly, at this resolution, the compact FD scheme without any numerical hyperviscosity is unstable, with Gibbs oscillations first generated at the shock front at earlier times (not shown) and then propagating out to contaminate the solution over the whole domain. The oscillations continue to grow and eventually render the solution meaningless for $t > 0.6$. With a numerical hyperviscosity $v_n = 1.0$, the Gibbs oscillations are suppressed near the shock front and decay with distance from the shock front. This remains so at later times. Note that this numerical viscosity is rather small in terms of the nondimensional ratio $v_nC(0)/v$, which is 0.0090. The best scheme is the hybrid scheme: due to the application of WENO to the shock region, no oscillation appears in the numerical solution. For these 1D calculations, we used a third-order total variation diminishing Runge–Kutta scheme [23].

The above confirms the necessity of using numerical viscosity in the central compact FD scheme and the effectiveness of our hyperviscosity formulation. It must be noted that the oscillations here are originated only from the Gibbs phenomenon, as no turbulent fluctuations exist in the region outside the shock. Not plotted here, we found that, for this particular problem, if the domain is resolved by more grid points (*e.g.*, 500), then all schemes are stable and give an acceptable solution.

4.2. Comparison with pseudo-spectral simulation in the nearly incompressible limit

As part of a systematic validation, we now briefly consider the nearly incompressible limit. A forced isotropic turbulence is simulated with $M = 0.1125$ and $Re = 70$, leading to a quasi-steady flow Reynolds number $Re_\lambda = 64.6$ and $M_t = 0.238$. Here the compact FD scheme is used for all regions in the flow, namely, WENO is switched off. The forcing function was made solenoidal to minimize the compressibility effect. At the statistically stationary stage, we indeed found that the compressibility effect is very small, as shown by the following ratios: $\rho'/\rho_0 = 0.019$, $\theta'/\omega' = 0.015$, and $(u^c)'/u' = 0.098$, where all properties with $'$ indicate rms component fluctuation level, u^c is the compressible component of the velocity field according to the Helmholtz decomposition [9]. Therefore, the flow may be viewed as nearly incompressible. Fig. 4 shows the average kinetic energy spectrum during the time interval of $7.3 \leqslant t/T_e \leqslant 14.6$ when the flow is statistically stationary. Also shown is the average energy spectrum from a standard pseudo-spectral simulation of incompressible turbulence, under the identical initial condition and flow Reynolds number. The excellent agreement shows that our compact FD scheme for compressible turbulence can reproduce the results of incompressible turbulence at small Mach number. We also found that the instantaneous flow fields from the two simulations are almost identical for $t < 3\tau$ and the instantaneous volume-averaged flow statistics are the same for $t < 3\tau$ (plots not shown here). Here $\tau \equiv L_f/u'$ is the large-eddy turnover time. These observations validate our compact FD code and confirm its near spectral accuracy as indicated in Section 3.3.1.

4.3. Tests with compact FD for low turbulent Mach number

We now discuss results related to test simulations for three-dimensional compressible turbulence at relatively low turbulent Mach numbers when there are no shocks and as such it is natural to apply just the compact FD to treat all regions. This ensures a uniform eighth-order accuracy and avoids issues related to the interfaces in the hybrid treatment. Here we consider a decaying compressible turbulence previously simulated by Samtaney et al. [9] using 10th-order central compact FD scheme. Following Samtaney et al. [9], the velocity field was initialized using a random field with a prescribed energy spectrum that is identical to Eq. (2.9) in Samtaney et al. [9] for their Run D4. The normalized temperature and density were simply initialized to one at all spatial points. The dimensionless parameters were $Re = 520$ and $M = 0.31$, yielding the initial turbulent Mach number M_t is 0.3 and the initial Taylor microscale Reynolds number Re_λ is 72. This corresponds exactly to Run D4 in Samtaney et al. [9]. For decaying compressible turbulence, as time evolves, both M_t and Re_λ decrease with time. Therefore, there is essentially no shocks in this flow. A 128^3 grid was applied.

Three runs were performed, as shown in the first three rows in Table 1. To mimic the work of Samtaney et al. [9], we also apply only the compact FD scheme to all regions. We found that, without any numerical hyperviscosity, our code became unstable after a few hundred steps. However, with a small numerical hyperviscosity ($\nu_n = 0.05$), our code was stable. Run 128DC1 in Table 1 is the base case. Run 128DC2 doubled the time step size relative Run 128DC1. Run 128DC3 is designed to test the sensitivity of the simulated flow on the level of numerical hyperviscosity, where ν_n is increased by a factor of 200 compared to that used in Run 128DC1.

Fig. 5 compares the longitudinal velocity derivative skewness and the dilatation from these three runs. The results of Run D4 from Samtaney et al. [9] are also shown for comparison. The results from Run 128DC1 and 128DC2 are indistinguishable, showing that the time steps used are indeed small enough and the 2nd-order Runge–Kutta time integration is accurate. Run 128DC3 produces essentially the same results in terms of the average dilatation, except that the skewness is slightly smaller in magnitude. All the results are in excellent agreement with those of Samtaney et al. [9]. The above demonstrate that our eighth-order central compact FD scheme was correctly implemented and its accuracy is comparable to the 10th-order central compact FD scheme used in Samtaney et al. [9]. Since central compact FD without any numerical dissipation is likely to be unstable [15,6]. The fact that a variation of ν_n by a factor 200 did not significantly alter the results shows that our numerical hyperviscosity scheme is highly effective yet has little effect on the overall accuracy of the method.

The above insensitivity to ν_n can be explained by the criterion given in Eq. (53). For $\nu_n = 0.05$ and $\nu_n = 10$, the ratio $\nu_n C(0)Re/\mu$ is roughly equal to 0.0001 and 0.02, respectively, based on the reference temperature. Therefore the criterion, Eq. (53), is well satisfied and as such the dynamics of large scales should not be noticeably affected by the numerical hyperviscosity term. Indeed, the criterion, Eq. (53) should be used to set up the value of ν_n and we recommend that the ratio $\nu_n C(0)Re/\mu$ be kept less than 1%. It is important to note that the criterion requires that the numerical hyperviscosity coefficient ν_n be decreased as Re is increased. The tests above show that our hyperviscosity formulation is very effective, namely, even a very small ν_n, as measured in terms of the ratio $\nu_n C(0)Re/\mu$, can ensure stability of the numerical method.

On the other hand, the effective viscosity applied to the highest wavenumber (*i.e.*, numerical noises resulting from the compact central FD itself) is $0.757\nu_n$. The ratio $0.757\nu_n/(\mu/Re)$ for $\nu_n = 0.05$ and $\nu_n = 10$ is 2.65 and 530, respectively. This, together with the ratio for most other small to moderate wavenumbers shown above, shows that the effective viscosity is a very strong function of scales of the fluctuations. This is precisely the reason for the effectiveness of our hyperviscosity formulation.

4.4. Comparison of the hybrid scheme with compact FD and WENO

Next, we performed three runs for decaying compressible turbulence (128DC4, 128DH1, 128DW1 in Table 1) at the initial turbulent Mach number of 0.56 and initial Taylor microscale Reynolds number of 72 by setting $Re = 520$ and $M = 0.58$. Other
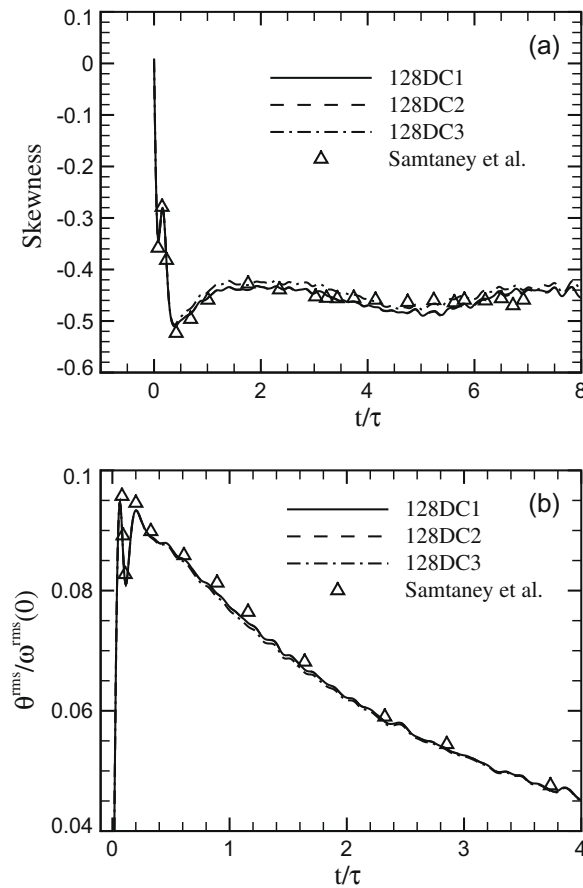
Fig. 5. Evolution of (a) longitudinal velocity derivative skewness and (b) dilatation for the decaying compressible turbulence at the initial $M_t = 0.3$.

setting and the initialization method are identical to the three runs discussed above. Again all were performed with 128^3 resolution. Run 128DC4 used the compact FD only for all regions, Run 128DH1 used the hybrid scheme, and Run 128DW1 used WENO for all grid points. In run 128DH1, about 10% of the grid points are treated with WENO, indicating occurrence of shocklets. It is assumed here, however, because of the relatively low flow Reynolds number which decreases with time, the shock regions have a thickness on the order of flow Kolmogorov scale [9] which increases with time. These conditions imply that the shock regions can be adequately resolved by the compact FD method alone as long as it is stable at early times. Because of the uniform eighth-order accuracy, the results from 128DC4 are then used as benchmark for other runs. A small hyperviscosity coefficient $v_n = 0.05$ was used in Run 128DC4 and 128DH1, no numerical viscosity was present in Run 128DW1. It is noted that this is about the highest M_t that our compact FD scheme alone can handle without numerical instability. We found that our compact FD alone could not simulate this decaying compressible turbulence at $M_t(0) = 0.6$ with the use of $v_n = 0.05$ due to numerical instability.

Fig. 6 displays the time evolution of longitudinal velocity derivative skewness and the dilatation for these three runs. Compared to results at $M_t(t = 0) = 0.3$ shown in Fig. 5, a much higher compressibility effect is observed in terms of the average dilatation. The velocity derivative skewness shows a stronger overshoot before settling down to a stationary state value. The average velocity derivative skewnesses for the time interval $3 < t/\tau < 8$ are -0.437, -0.435, -0.430, respectively, for runs 128DC4, 128DH1, 128DW1. Again $\tau \equiv L_f/u'$ is the large-eddy turnover time. The compact FD yields the highest dilatation, while WENO has the smallest dilatation. The hybrid scheme gives a dilatation very close to the compact scheme, except during a period of about 2 eddy turnover times immediately after the peak dilatation where the hybrid method predicts a dilatation about 7.0–5.0% smaller than that of the compact FD method; at longer times ($t/\tau > 3$), this difference is reduced to 5.0–3.0%. WENO, on the other hand, underpredicts the dilatation by 15.5–12.0% at long times, relative to the compact FD method.

A much clear demonstration of the advantage of our hybrid scheme over WENO is shown in Fig. 7 where we compare the simulated kinetic energy spectra from the three runs. Our hybrid scheme yields a kinetic energy spectrum very close to the compact FD scheme, but WENO, due to its highly dissipative nature, gives a much faster decay of energy at higher wavenumbers. This is consistent with the observation made in Larsson et al. [13].

Lastly, we compare the probability density distributions of two selected quantities in Fig. 8. Again assuming the results of the compact FD run (128DC4) can be used as a benchmark, it is evident that the hybrid method is more accurate in capturing the large amplitude fluctuations than the WENO method alone. Probability density distributions of other variables (not shown here) also lead to the similar conclusion.
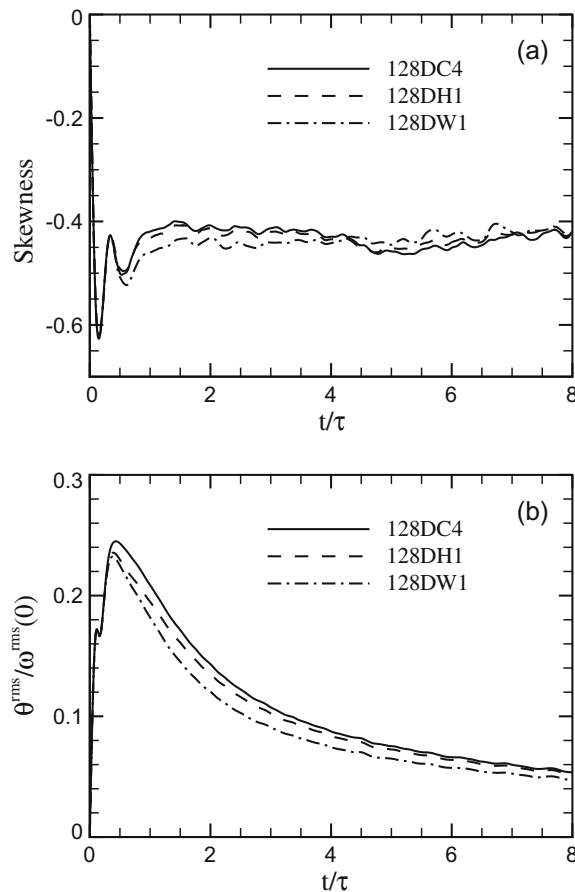
Fig. 6. Evolution of (a) longitudinal velocity derivative skewness and (b) dilatation for the decaying compressible turbulence at the initial $M_t = 0.56$.
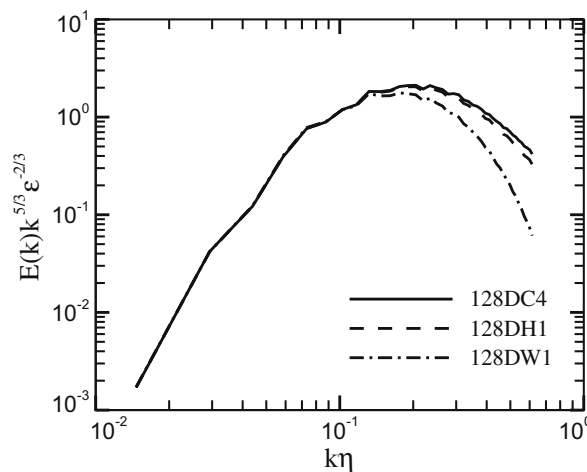

Fig. 7. Kinetic energy spectrum at $t = 2.0\tau$.

In summary, the compact FD has the best overall accuracy but is the least stable, while WENO is the most stable scheme but has excessive dissipation. Our hybrid scheme appears to combine the best features of the two to yield a relatively accurate and stable scheme for compressible turbulence simulations.

4.5. Forced compressible turbulence and the effect of cooling function

Now we shall consider a few simulations for forced compressible turbulence with even higher turbulent Mach numbers by setting $Re = 70$ and $M = 0.6$. First we consider the three runs at 128^3 resolutions shown in Table 2. Here Re_λ and M_t represent, respectively, the Taylor microscale Reynolds number and turbulent Mach number averaged over time when the flow
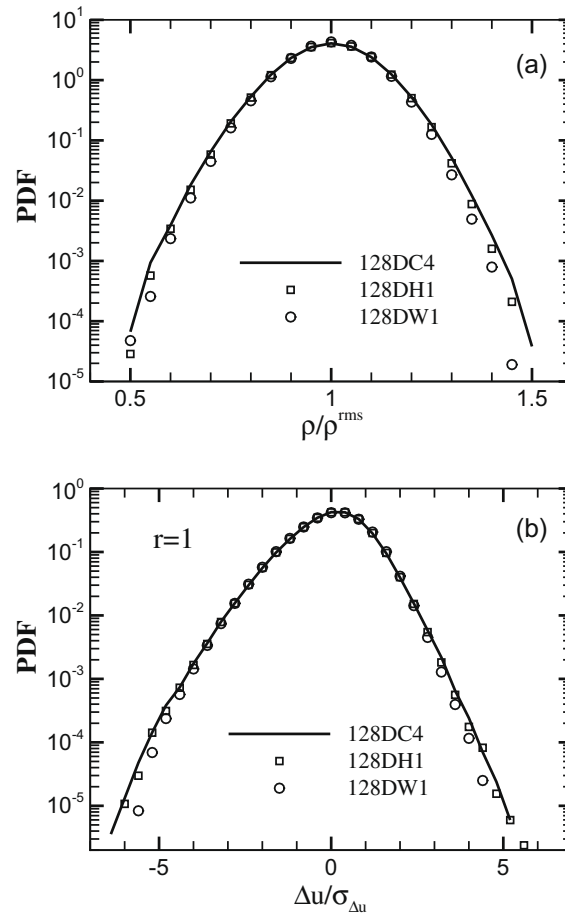
Fig. 8. Comparison of probability density distributions of (a) local density and (b) longitudinal velocity increment at a separation equal to $r\,dx$ with $r = 1$. The time considered is $t/\tau = 1.0$.

Table 2
Runs and parameters for forced compressible turbulence.

Run no.	Method	Re_λ	M_t	v_n	dt/τ
128FI	Hybrid	61.1	1.27	0.05	0.001
128FII	Hybrid	61.7	1.27	0.05	0.001
128FIII	Hybrid	62.1	1.27	0.05	0.001

reaches the statistically stationary stage. At $M_t = 1.27$, only the hybrid scheme is the viable approach. The three runs 128FI, 128FII, and 128FIII correspond to the three cooling functions shown in Eq. (38). The velocity field is forced by fixing the total kinetic energy in the first two wavenumber shells to $E_K(1) = 1.242477$ and $E_K(2) = 0.391356$ and the forcing field is made incompressible. An identical initial flow was used and was generated by first running 128FI for about 10 eddy turnover times. The time was then reset to zero and the three different cooling functions were applied to generate the results for the three runs.

It was found that for these runs at $M_t = 1.27$, up to 13% of the grid points fall into the shock regions. Fig. 9 compares the time evolution of space-averaged longitudinal velocity derivative skewness and the dilatation. The normalized dilatation has a rather high mean value of around 0.55 and the skewness has a mean value around −2.0. Such a large magnitude of velocity derivative skewness is not possible for incompressible turbulence, and results from very strong compression across the shocklets. Fig. 9 shows that the stronger the nonuniformity in the cooling rate (type III cooling is most nonuniform and type I is completely uniform), the weaker the discontinuity across the shocklets as indicated by the somewhat smaller magnitudes in dilatation and skewness. The average skewness for runs 128FI, 128FII, and 128FIII in $3 < t/\tau < 5$ are −2.00, −1.85, −1.71, respectively. This can be qualitatively explained by the reduction in jumps across the shock associated with the nonuniform cooling: stronger cooling on the lower speed/high temperature side (the rear of shock) and weaker cooling on the higher speed/lower temperature side (the front of shock).

Nevertheless, the relative differences in the dilatation and skewness among these three cooling functions are typically less than 15%. Furthermore, the resulting kinetic energy spectra are almost identical, as shown in Fig. 10. We thus conclude that the results are not very sensitive to the exact form of the cooling function used.
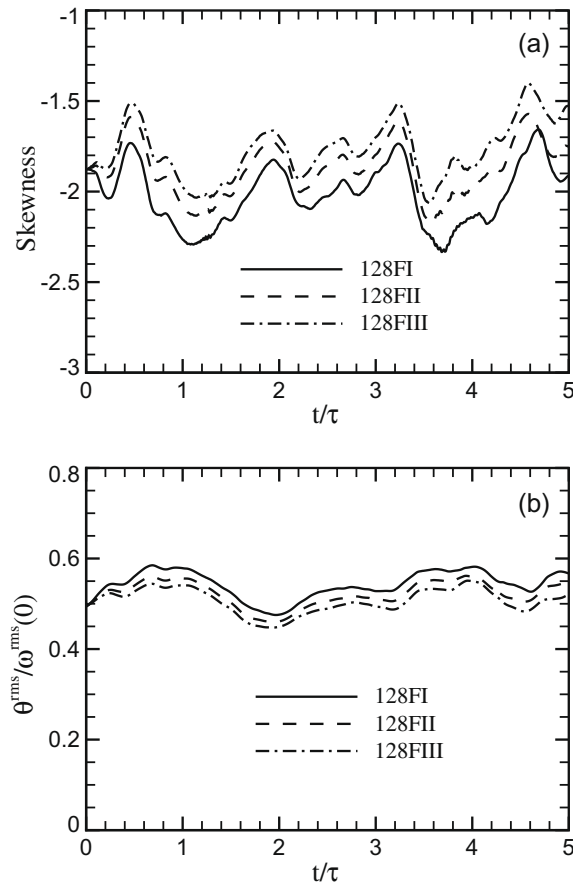
Fig. 9. Evolution of (a) longitudinal velocity derivative skewness and (b) dilatation for the forced compressible turbulence with average turbulent Mach number of M_t = 1.27.
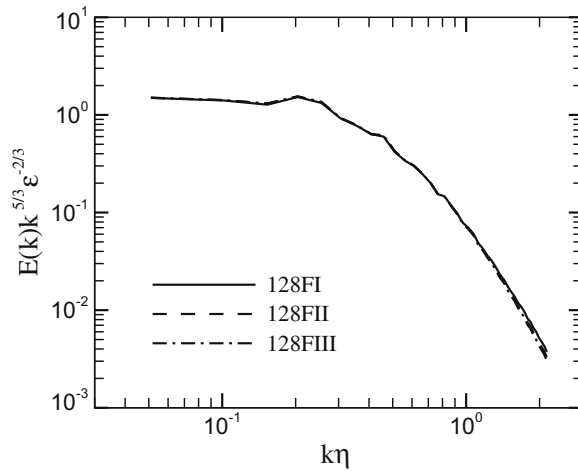

Fig. 10. Kinetic energy spectrum averaged over the time interval $3 \leqslant t/\tau \leqslant 5$.

4.6. Sensitivity to the threshold value R_θ used to define the shock region

In this section, we shall vary the threshold value R_θ used to define the shock region to examine if the statistics of the simulated compressible turbulence is sensitive to R_θ. Table 3 shows the different R_θ values used and the key resulting flow statistics including the average Taylor microscale Reynolds number Re_λ, the turbulent Mach number M_t, the velocity derivative skewness S, and the rms fluctuation level of the dilatation normalized by the rms vorticity at the initial time. In all these runs, the hybrid method is used. Note that Run 128R3 listed in Table 3 is identical to Run 128F1 listed in Table 2, namely, the

Table 3
Setting and results with different threshold values used to define the shock region.

Run no. (R_θ)	WENO region (%)	Re_λ	M_t	S	$\theta^{rms}/\omega^{rms}(0)$
128R1 ($R_\theta = 1$)	38.0	61.3	1.27	−2.00	0.554
128R2 ($R_\theta = 2$)	17.4	61.2	1.27	−1.99	0.553
128R3 ($R_\theta = 3$)	11.2	61.1	1.27	−2.00	0.557
128R4 ($R_\theta = 4$)	7.75	61.0	1.27	−2.02	0.559
128R5 ($R_\theta = 5$)	5.46	60.8	1.27	−2.05	0.562

settings for dt and v_n follow those of Run 128F1. Each simulation is done for 5 eddy turnover times starting from an identical, developed flow field, and the averaged statistics are obtained using the time window from 3 to 5 eddy turnover times.

As R_θ is raised from 1 to 5, the percentage of spatial region treated by WENO is reduced from 38.0% to 5.46%. However, the resulting flow statistics are rather insensitive to the value of R_θ for the range of R_θ tested here.

Fig. 11 compares the velocity derivative skewness and the r.m.s. value of velocity divergence. Only a very minor deviation is seen for Run 128R5 from other runs, indicating that a value of $R_\theta = 5$ is perhaps a bit too larger and some of the strong shock regions may not be treated by WENO. The same conclusion is reached when the energy spectra are compared in Fig. 12.

In conclusion, the results are insensitive to R_θ for $1 \leqslant R_\theta \leqslant 4$, showing that R_θ needs not to be optimized for our hybrid method. A value of $R_\theta = 2$ or $R_\theta = 3$ is recommended, which is consistent to $R_\theta = 3$ chosen by Samtaney et al. [9] in their post processing of shock regions.

4.7. High-resolution simulation at high turbulent Mach number

As yet another demonstration of our hybrid method, we conducted a run (Run 512FI in Table 2) at both relatively high Reynolds number ($Re_\lambda = 177$) and Mach number ($M_t = 1.08$), at 512^3 grid resolution with $Re = 500$ and $M = 0.45$. To our
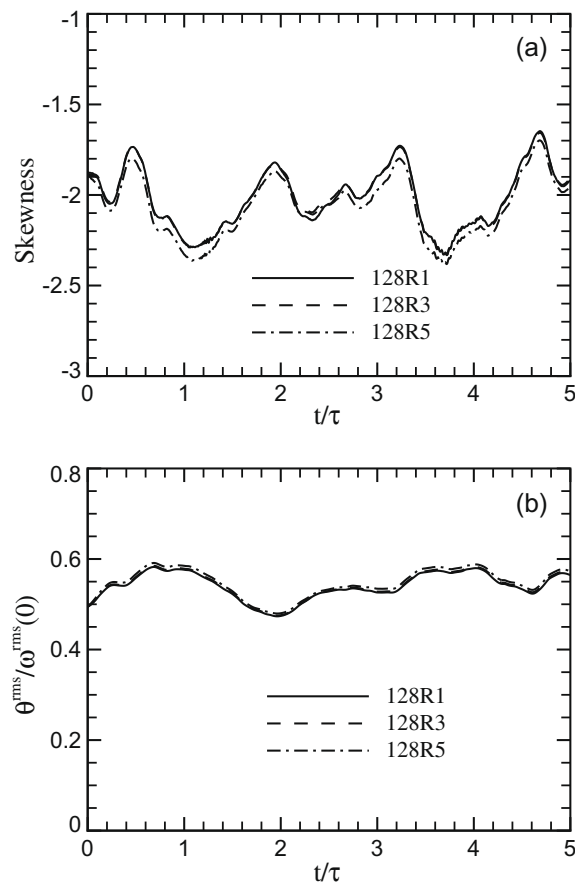

Fig. 11. Evolution of (a) longitudinal velocity derivative skewness and (b) dilatation for the forced compressible turbulence, for runs with different R_θ values.
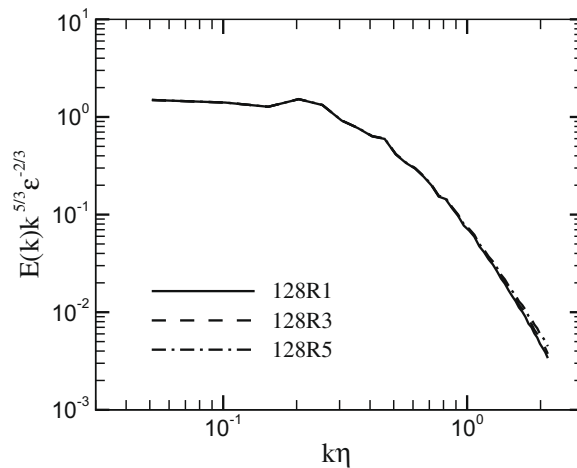
Fig. 12. Kinetic energy spectrum averaged over the time interval $3 \leqslant t/\tau \leqslant 5$, for runs with different R_θ values.

knowledge, this is the highest turbulent Mach number ever simulated at this resolution using a hybrid approach of the type discussed here. In this simulation, the forcing field is defined using the complete Fourier modes (namely, no projection is applied to the forcing function) in low wavenumber shells. This has the tendency of enlarging velocity divergence and as such leads to more intense and a larger number of shock front regions. To save computational time, we first performed a forced compressible turbulence at grid resolution of 256^3. After about five eddy turnover times, the 256^3 flow was then used to initialize the 512^3 simulation. The first type of cooling function was used. The time step size and the numerical viscosity were set to $dt = 0.0003$ and $v_n = 0.02$.

In Figs. 13 and 14, we show the density contours and dilatation contours on an arbitrarily selected $x - y$ slice at a time instant when the flow is stationary. Severe discontinuities (red-blue interfaces) in the density contour plot represent shocklets. The sheetlike, narrow blue regions where the dilatation is largely negative (Fig. 14) also imply shocklets. Figs. 14 shows the existence of both relatively flat shocklets and highly curved shock fronts. In sharp contrast, the expansion regions (positive dilatation) tend to be bloblike round regions. These compressible flow structures are qualitatively similar to what had been observed in previous studies [29,9,30].

While it is beyond the scope of the current paper to discuss in depth the flow structure and dynamics associated with compressible turbulence, we shall very briefly explore the jump conditions across moving and unsteady shocklets in run 512F1. It has been postulated [9] that the Rankine–Hugoniot jump conditions for a normal plane shock apply to the shocklets in compressible turbulence. For example, the pressure jump and density jump across an inviscid, normal, plane shock are related by

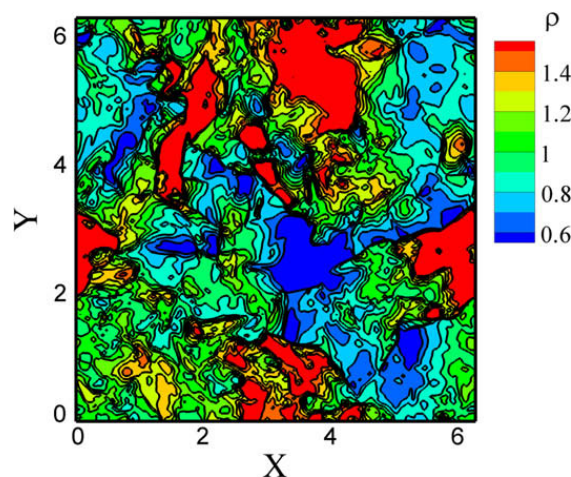$$\rho_r = \frac{(\gamma + 1)p_r + \gamma - 1}{(\gamma - 1)p_r + \gamma + 1}, \tag{66}$$

Fig. 13. Density contours on a slice for a forced compressible turbulence at $M_t = 1.08$ and $R_\lambda = 177$, simulated with 512^3 grid resolution.
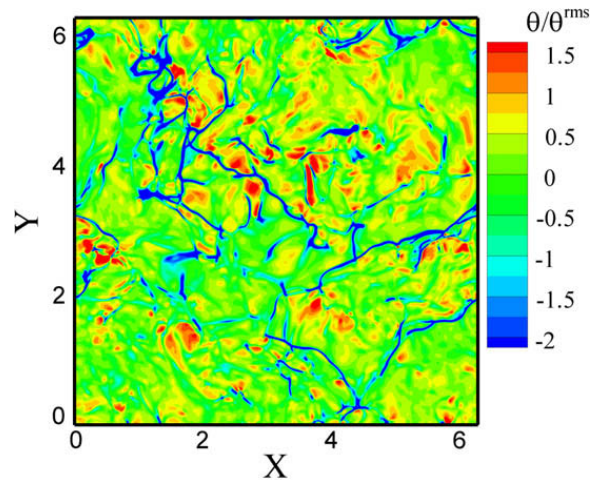
Fig. 14. Dilatation contours on the same slice used for Fig. 13.

where $\rho_r = \rho_2/\rho_1$ and $p_r = p_2/p_1$, with the subscripts "1" and "2" refer to the front and rear of the shock, respectively. The velocity jump in the direction normal to the shock front, across a normal shock, can be written as

$$|u_{2n} - u_{1n}| = \sqrt{\frac{2(p_2 - p_1)^2}{\rho_1[(\gamma + 1)p_2 + (\gamma - 1)p_1]}}. \tag{67}$$

The normal direction is directed from the rear side to the front side of a shocklet.

To examine whether the above conditions apply to the shocklets in the compressible turbulence, we need to extract the shocklets and also identify the exact location of the shocklet front. We follow the method of Samtaney et al. [9] that defines the shock surface by the following two conditions:

$$\nabla^2 \rho = 0 \quad \text{and} \quad -\theta > 3\theta'. \tag{68}$$

Note that the second condition defines the shock front of finite width, while the first condition precisely specifies a center surface in the front region.

Fig. 15 shows a scatter plot of $\rho_r - 1$ versus $p_r - 1$ for 2000 line elements passing through shocklets in the normal direction. The line represents the theoretical relation given by Eq. (66). The figure shows a high degree of agreement between the data and the Rankine–Hugoniot relation, although the viscous and curvature effects [31] are not considered in this Rankine–Hugoniot relation.

We also compare the normal velocity jump across the shocklets from the simulation to that predicted by Eq. (67) using a scatter plot in Fig. 16. On average, they are in reasonable agreement and the correspondence improves with the shocklet strength.

The above discussions reveal that the compressible turbulence we have simulated at relatively high Mach numbers and Reynolds numbers are consistent with known physical descriptions associated with shocklets in isotropic turbulence.
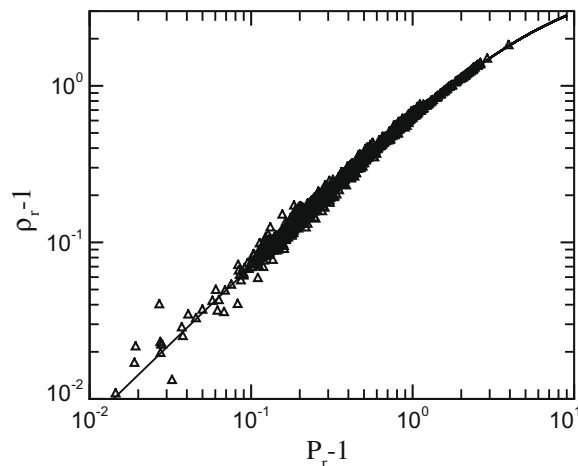

Fig. 15. Density ratio versus pressure ratio in the direction normal to the extracted shocklets. 2000 points were used in the scatter plot.
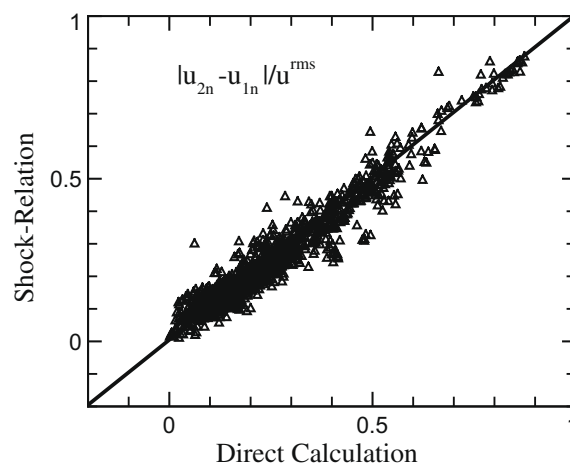
Fig. 16. Normal velocities differences across shocklets. 2000 points were used in the scatter plot.

5. Summary and conclusions

Numerical simulation of compressible turbulence presents new challenges due to molecular-scale discontinuities (i.e., shocklets) associated with strong local compression, as well as their interactions with intermittent small-scale turbulent structures. Often it is not computationally feasible to directly resolve the physical scales of shocklets. Due to physical conservation laws, it is usually assumed that the dynamics of shocklets is basically unchanged as long as the thickness of shocklets are kept reasonably small. Indeed, it can be shown that the total amount of dissipation across the shock is, for small viscosity, independent of viscosity, and dependent only on the jump conditions across the shock [32]. Put it another way, while numerical viscosity smears the shock discontinuity, it does not alter the total amount of dissipation when integrated across the shock. WENO is known to preserve shock relations [10–12], although the thickness of shock is 2–3 grid lengths in numerical simulations. We have also found that most of our results are not sensitive to grid refinement, except local differences in the shock regions as expected due to different effective shock thicknesses for different grid resolutions. Furthermore, at moderate Mach numbers, our hybrid results reproduce central FD (without the WENO treatment), implying that the shock region treatment has negligible effect on the dynamics of flow outside shock regions. These observations combined with the fact that all dynamics are directly resolved in smooth regions make our scheme essentially a *direct numerical simulation* for scales of the order of a few Kolmogorov scales and larger. While we did not use the term DNS here, we note that others did use it previously when WENO was used to treat the shock regions [33–35].

The general idea of combining compact FD scheme and WENO to form a hybrid scheme is not new, and has been investigated by others [14–17]. But the development to date has not met the desire to simulate compressible turbulence at both relatively high turbulent Mach numbers and Reynolds numbers. This is because there are several subtle physical and numerical issues associated with combining the two schemes. In this paper, we have developed a hybrid compact FD and WENO scheme for compressible turbulence using a flux-based conservative and formally consistent formulation. The conservative form preserves rigorous flux conditions across the interface leading to physically correct jump conditions across a shock, and the consistent formulation makes it computationally more efficient as the whole computational domain can be treated together. They together ensure an optimal connection between the shock regions and the smooth regions at the interface.

Furthermore, a novel numerical hyperviscosity treatment is developed to dissipate unwanted small-scale fluctuations in the smooth regions without affecting the accuracy of the overall approach in the smooth regions. A thorough and insightful analysis of the hyperviscosity formulation in both Fourier space and physical space is presented to show the effectiveness of the formulation in improving numerical stability, without compromising the accuracy of the hybrid method. Finally, this hyperviscosity term is implemented in a way that is consistent with the conservative formulation and makes no contribution to the shock regions treated by WENO. The theoretical analysis is confirmed by numerical tests for both one dimensional problem and 3D compressible turbulence. Combining the analysis and test simulations, we also developed a criterion to guide the specification of numerical hyperviscosity coefficient (the only adjustable coefficient in the formulation). While it is not shown in this paper, we found that the hyperviscosity formulation can also be applied to compact central FD schemes at other even orders.

Test simulations demonstrated that the advantages of the high-order compact FD and WENO are preserved in our hybrid scheme, making it possible to simulate accurately compressible turbulence at a turbulent Mach number larger than one. We have successfully simulated a forced compressible turbulence at M_t = 1.08 and Re_λ = 177 on a 512^3 grid. This will allow a systematic analysis of the statistics and dynamics of the simulated compressible turbulence in terms of turbulent Mach numbers and flow Reynolds numbers, which will be documented in forthcoming papers. Our hybrid scheme retains the dissipative feature of WENO for shock fronts but is essentially non-dissipative away from the shock regions. To our knowledge, compressible turbulence at 512^3 grid resolution with larger than one turbulent Mach number has not been attempted

with the type of hybrid scheme we proposed here. Previously, PPM (Piecewise Parabolic Method) has been used to simulate flows at high turbulent Mach numbers [36,37], but it is known that PPM is very dissipative and the physical flow Reynolds number cannot be precisely defined due to excessive level of numerical dissipation.

We also briefly studied the effect of large-scale thermal forcing (both spatially uniform and nonuniform cooling) and concluded that the overall dynamics of the flow is not so sensitive to the type of cooling function used.

In this study we have chosen to design our hybrid scheme by combing an eighth-order compact FD and a seventh-order WENO. Certainly, other orders of compact FD and WENO can be employed, along with a similar approach for the numerical viscosity formulation. Our experience shows that, provided that an adequate grid resolution is used, a similar accuracy may be obtained by lower-order methods for simulations at moderate turbulent Mach numbers and low flow Reynolds numbers when the shock fronts have a thickness comparable to Kolmogorov scales [9]. For small turbulent Mach numbers, say $M_t < 0.3$, reduction of the orders could make the representation of the thermodynamic quantities less accurate, simply due to the relatively small magnitude of fluctuations of thermodynamic variables. For high Mach-number and high Reynolds-number flows, the shock fronts are not directly resolved, a higher-order WENO would capture more accurately the jumps across shock fronts.

Finally, we should note that an implicit assumption for all hybrid simulation methods of the kind used here is that the structure and dynamics of compressible turbulence are not sensitive to the local dissipative nature of WENO at shock fronts. In other words, since the grid spacing is on the order of the Kolmogorov scale of turbulence and the effective thickness of shocklets is also similar to grid spacing, the underlying assumption is the dynamics of compressible turbulence is unaltered even when the shock thickness is made as large as the flow Kolmogorov scale. At the current stage, the question whether such an underlying working assumption is valid or not remains to be investigated.

Acknowledgments

References

[1] P. Moin, K. Mahesh, Direct numerical simulation: a tool in turbulence research, Annu. Rev. Fluid Mech. 30 (1998) 539–578.
[2] L.-P. Wang, S. Chen, J.G. Brasseur, J.C. Wyngaard, Examination of hypotheses in Kolmogorov refined turbulence theory through high-resolution simulations. Part 1. Velocity field, J. Fluid Mech. 309 (1996) 113–156.
[3] S.K. Lele, Compact finite difference schemes with spectral-like resolution, J. Comput. Phys. 103 (1992) 16–42.
[4] K. Mahesh, A family of high order finite difference schemes with good spectral resolution, J. Comput. Phys. 145 (1998) 332–358.
[5] J.A. Ekaterinaris, Implicit, high-resolution, compact schemes for gas dynamics and aeroacoustics, J. Comput. Phys. 156 (1999) 272–299.
[6] T.K. Sengupta, G. Ganeriwal, S. De, Analysis of central and upwind compact schemes, J. Comput. Phys. 192 (2003) 677–694.
[7] T.K. Sengupta, G. Ganerwal, A. Dipankar, High accuracy compact schemes and Gibbs' phenomenon, J. Sci. Comput. 21 (2004) 253–268.
[8] T.K. Sengupta, R. Jain, A. Dipankar, A new flux-vector splitting compact finite volume scheme, J. Comput. Phys. 207 (2005) 261–281.
[9] R. Samtaney, D.I. Pullin, B. Kosovic, Direct numerical simulation of decaying compressible turbulence and shocklet statistics, Phys. Fluids 5 (2001) 1415–1430.
[10] C.W. Shu, S. Osher, Efficient implementation of essentially non-oscillatory shock-capturing schemes, J. Comput. Phys. 77 (1988) 439–471.
[11] G.S. Jiang, C.W. Shu, Efficient implementation of weighted ENO schemes, J. Comput. Phys. 126 (1996) 202–228.
[12] D.S. Balsara, C.W. Shu, Monotonicity preserving weighted essentially non-oscillatory schemes with increasingly high order of accuracy, J. Comput. Phys. 160c (2000) 405–452.
[13] J. Larsson, A. Cook, S.K. Lele, P. Moin, B. Cabot, B. Sjogreen, H. Yee, H. Zhong, Computational issues and algorithm assessment for shock/turbulence interaction problems, J. Phys.: Conf. Series 78 (2007) 012014.
[14] N.A. Adams, K. Shariff, A high-resolution hybrid compact-ENO scheme for shock–turbulence interaction problems, J. Comput. Phys. 127 (1996) 27–51.
[15] S. Pirozzoli, Conservative hybrid compact-WENO schemes for shock–turbulence interaction, J. Comput. Phys. 178 (2002) 81–117.
[16] Y.X. Ren, M. Liu, H. Zhang, A characteristic-wise hybrid compact-WENO scheme for solving hyperbolic conservation laws, J. Comput. Phys. 192 (2003) 365–386.
[17] Q. Zhou, Z. Yao, F. He, M.Y. Shen, A new family of high-order compact upwind difference schemes with good spectral resolution, J. Comput. Phys. 227 (2007) 1306–1339.
[18] D.J. Hill, D.I. Pullin, Hybrid tuned center-difference-WENO method for large eddy simulations in the presence of strong shocks, J. Comput. Phys. 227 (2004) 435–450.
[19] D. Kim, J.H. Kwon, A high-order accurate hybrid scheme using a central flux scheme and a WENO scheme for compressible flowfield analysis, J. Comput. Phys. 210 (2005) 554–583.
[20] J. Larsson, B. Gustafsson, Stability criteria for hybrid difference methods, J. Comput. Phys. 227 (2008) 2886–2898.
[21] W. Sutherland, The viscosity of gases and molecular force, Philos. Mag. S5 (36) (1992) 507–531.
[22] J.O. Hinze, Turbulence, second ed., McGraw-Hill, New York, 1975. pp. 175–250.
[23] S. Gottlieb, C.W. Shu, Total variation diminishing Runge–Kutta schemes, Math. Comput. 67 (1998) 73–85.
[24] T.A. Zang, R.B. Dahlburg, J.P. Dahlburg, Direct and large-eddy simulations of three-dimensional compressible Navier–Stokes turbulence, Phys. Fluids. A 4 (1992) 127–140.
[25] D.H. Porter, P.R. Woodward, A. Pouquet, Inertial range structures in decaying compressible turbulent flows, Phys. Fluids 10 (1998) 237–245.
[26] S. Kida, A.S. Orszag, Energy and spectral dynamics in forced compressible turbulence, J. Sci. Comput. 5 (1990) 85–125.
[27] T. Passot, E. Vazquez-Semadeni, A. Pouquet, A turbulent model for the interstellar medium. II. Magnetic fields and rotation, Astrophys. J. 455 (1995) 536–555.

[28] S. Chen, G.D. Doolen, R.H. Kraichnan, Z.-S. She, On statistical correlations between velocity increments and locally averaged dissipation in homogeneous turbulence, Phys. Fluids A 5 (1993) 458–463.

[29] S. Lee, S.K. Lele, P. Moin, Eddy shocklets in decaying compressible turbulence, Phys. Fluids 3 (1991) 657–664.

[30] S. Pirozzoli, F. Grasso, Direct numerical simulations of isotropic compressible turbulence: influence of compressibility on dynamics and structures, Phys. Fluids 16 (2004) 4386–4407.

[31] A.G. Bashkirov, Influence of viscous stresses on shock wave stability in gases, Phys. Fluids A 3 (1991) 960–966.

[32] T. Colonius, F. dAuria, C.E. Brennen, Acoustic saturation in bubbly cavitating flow adjacent to an oscillating wall, Phys. Fluids 12 (2000) 2752–2761.

[33] M.P. Martin, E.M. Taylor, M. Wu, V.G. Weirs, A bandwidth-optimized WENO scheme for the effective direct numerical simulation of compressible turbulence, J. Comput. Phys. 220 (2006) 270–289.

[34] E.M. Taylor, M.P. Martn, Stencil adaptation properties of a WENO scheme in direct numerical simulations of compressible turbulence, J. Sci. Comput. 30 (2007) 533–554.

[35] E.M. Taylor, M. Wu, M.P. Martin, Optimization of nonlinear error for weighted essentially non-oscillatory methods in direct numerical simulations of compressible turbulence, J. Comput. Phys. 223 (2007) 384–397.

[36] P. Colella, P.R. Woodward, The piecewise parabolic method (PPM) for gas-dynamical simulations, J. Comput. Phys. 54 (1984) 174–201.

[37] D. Porter, A. Pouquet, P. Woodward, Measures of intermittency in driven supersonic flows, Phys. Rev. E 66 (2002) 026301.